

Differential Microlensing Measurements of Quasar Broad Line Kinematics in Q2237+0305

M. O’Dowd^{1*}, N. F. Bate², R. L. Webster², R. Wayth³, K. Labrie⁴

¹*Columbia University, New York, NY, USA*

²*The University of Melbourne*

²*Harvard*

³*Gemini*

Accepted 2010 November 28

ABSTRACT

The detailed workings of the central engines of powerful quasars remain a mystery. This is primarily due to the fact that, at their cosmological distances, the inner regions of these quasars are spatially unresolvable. Reverberation mapping is now beginning to unlock the physics of the Broad Emission Line Region (BELR) in nearby, low-luminosity quasars, however it is still unknown whether this gas is dominated by virial motion, by outflows, or infall. The challenge is greater for more distant, powerful sources due to the very long response time of the BELR to changes in the continuum. We present a new technique for probing the kinematic properties of the BELR and accretion disk of high- z quasars using differential microlensing, and show how substantial information can be gained through a single observation of a strongly-lensed quasar using integral field spectroscopy. We apply this technique to GMOS IFU observations of the multiply-imaged quasar Q2237+0305, and find that the observed microlensing signature in the CIII] broad emission line favours gravitationally-dominated dynamics over an accelerating outflow.

Key words: broad line regions – microlensing – quasars: individual (Q 2237+0305)

1 INTRODUCTION

Differential microlensing offers the promise of indirectly measuring the spatial size and kinematics of different emitting regions in quasars. In this paper, a new observation of differential microlensing between the continuum and different velocity components of the CIII] broad line emission line in Q2237+0305 is presented. These data are then used to constrain the kinematics of the broad line gas.

The core regions of quasars are unresolved at any wavelength, and so physical understanding must be based on theoretical models constrained by their observed spectral properties. The gas responsible for the broad emission lines presents a particular challenge as there are relatively few measurements capable of even beginning to probe its kinematical structure. As such, there is still no agreement on even the simplest models of this structure. Beyond the obvious width of the emission lines, which indicate large Doppler velocities of tens of thousands of km/sec, most of our current understanding has come from reverberation mapping and from polarisation observations of emission lines. The most recent reverberation signatures have been interpreted

as arising from outflowing, inflowing and virialised motions (Denney *et al.* 2009; Bentz *et al.* 2009), while the polarisation studies have indicated an outflowing helical motion in the emission line gas (Young *et al.* 2007). Theoretical models have favoured outflowing winds (eg Murray & Chiang 1997), but alternative points of view are still under active consideration (eg. Gaskell 2009).

Differential microlensing provides an independent probe of the inner structure of quasars. In quasars that are subject to strong gravitational lensing, the BELR and potentially the accretion disk are resolved on the spatial scale of the fine magnification structure of the lens. Given a model for the lensing galaxy, observation of differential magnification between these components allows constraints to be placed on their sizes.

The use of this technique was first discussed by Nemiroff (1988), who specifically looked at the effect of a single low mass star on a range of kinematical models for the broad emission line region (BELR). A key result of this paper was that different parts of the emission lines were differentially magnified, depending on the kinematical model: in general the smaller spatial regions showed the greatest variations, as would be expected. Schneider & Wambsganss (1990) further considered the problem, noting that, in the case of a

* E-mail: matt@astro.columbia.edu

macro-imaged quasar, the differences between the lines in different images can be used to test whether particular emitting regions are being significantly microlensed. In particular, these authors noted that Keplerian motions in the BELR would be much easier to detect than infall (or presumably outflow). A key improvement in the modelling compared to Nemiroff (1988) was the use of microlensing magnification patterns to model the possible statistical variations for each macro-image. Schneider & Wambsganss (1990) also noted that differential microlensing would also effect the redshift measured from a particular line. More recently Abajas *et al.* (2007) and Lewis & Ibata (2004) both considered different signatures which might be induced in the observed structure of the broad emission lines.

There are at least four differential microlensing experiments which could allow the measurement of the physical parameters of the quasar emission regions. Target-of-opportunity observations of a quasar crossing a caustic provide the cleanest imaging experiment (Wyithe *et al.* 2000). The physical interpretation of a caustic crossing event is straightforward. However in order to trigger the target-of-opportunity, regular monitoring is required; and for a reasonable annual probability of observing a caustic crossing, more than ten objects would need to be monitored. Recently, monitoring data has been used to fit the size of the region emitting the quasar continuum using Bayesian Monte Carlo methods (Kochanek 2004; Eigenbrod *et al.* 2008b). These analyses rely on detailed modeling where a standard accretion disk is convolved with microlensing networks. A third and more specialized possibility arises when two macro-images straddle a caustic. In a surprising number of cases, the fluxes of the two images differ, while theory predicts them to be the same. Several variables in the modeling can affect the relative fluxes, but the size of the emission region is the dominant factor (Congdon *et al.* 2007; Bate *et al.* 2007). Bate *et al.* (2007) have shown that measurements of the anomalous fluxes can be used to set limits on the size of the emission regions.

The final method uses spectroscopic data to compare the shapes of emission lines and continuum spectra. If the broad emission line region has ordered kinematical motions, then differential magnification may change the shape of the emission lines of one image. In the case of a macro-imaged quasar, differences between the line spectra of the images can then provide a diagnostic for the kinematical motions of the broad emission lines. Such differences have already been observed in several sources (e.g. Keeton *et al.* 2006; Eigenbrod *et al.* 2008b; Sluse *et al.* 2008; Hutsemékers *et al.* 2010). In this work we apply this last method to new integral field spectroscopy (IFS) of the multiply imaged quasar Q2237+0305 (Huchra *et al.* 1985).

Q2237+0305 is an ideal candidate for differential microlensing experiments. The close proximity of the lensing galaxy, at $z_d = 0.0394$ compared to the quasar redshift of $z_s = 1.695$, yields a large projected Einstein Radius (ER) of $\sim 2 \times 10^{17} h_{70}^{1/2} (M/M_\odot)^{1/2} \text{cm}$ in the source plane. This ER, which characterizes the size-scale of magnification fluctuations, is significantly larger than its estimated continuum region size of $3 \times 10^{16} h_{70}^{1/2} (M/M_\odot)^{1/2} \text{cm}$ (Witt, Mao & Schechter 1995), and it is similar to the upper size limit of its CIII] and MgII BELR, determined from our previous observations of differential microlensing in this

source (Wayth *et al.* 2005, hereafter W05). This indicates a high probability of differential microlensing between continuum and broad lines, and also a reasonable probability of differential microlensing *within* the BELR.

Differential microlensing between the continuum and BELR in Q2237+0305 has been observed many times. Microlensing within the broad line itself has also been observed. Most notably, Eigenbrod *et al.* (2008) have conducted VLT monitoring of Q2237+0305 that spans several years, and present high quality slit spectroscopy of both continuum and BELR change, comparable to the data presented in this paper. However IFS observations can provide more reliable spectra as they allow more careful deblending of the small-separation lensed images and lensing galaxy.

Interpretation of the differences between the spectra of the four images requires a model for both the accretion disk and the spatial and kinematical structure of the BELR. Broadly, larger flux changes are expected for regions closer to the accretion disk. The velocity structure, projected along the line-of-sight to the quasar should discriminate between models where the higher velocities are far from the disk (due to an accelerating wind) and those where a high velocity might be found close to the disk (due to Keplerian motion around the central black hole). It is still not known which (if either) of these two models best describes the kinematics of the BELR.

The current work does not attempt to construct a fully consistent model of the BELR, nor include a full photoionisation calculation. Rather, a more limited question is addressed: near the accretion disk where the continuum is emitted, is the BELR gas moving relatively quickly or slowly? Answering this question will help resolve the dominant physical process in the inner BELR.

In Section 2 of this paper we present the observational data, and the methods of data reduction and spectra extraction. Section 3 describes the flux ratios for different emission lines and at different wavelengths for the continuum. In Section 4 we present simple models to describe the BELR kinematics. Section 5 describes the computation of the microlensing simulations which are convolved with the models. In Section 6, the results of comparing the model predictions with the data are presented. These are discussed in Section 7, with the final conclusions presented in Section 8.

2 OBSERVATIONAL DATA

Q2237+0305 was observed on the 27th of June 2006 with the GMOS Integral Field Unit (IFU) (Allington-Smith *et al.* 2002; Hook *et al.* 2004) on the Gemini South telescope (program ID: GS-2006A-Q-14). 5×15 minute exposures were taken in one-slit mode using the B600 grating and with central wavelength 515 nm, giving a spectral range of 3975Å to 6575Å and a resolution of $R = 1688$. At Q2237+0305's redshift of 1.69, this covers the CIII] and CIII] broad emission lines. Seeing conditions were excellent, with a PSF FWHM of $0''.6$.

The GMOS IFU in one-slit mode gives a $5'' \times 3''.5$ field of view, with an additional $5'' \times 1''.25$ field offset by ~ 1 arcmin to measure the sky. Importantly, the field is 'filled', with the science field consisting of 500 $0''.2$ diameter hexagonal lenslets with abutting edges. The filled field means that no

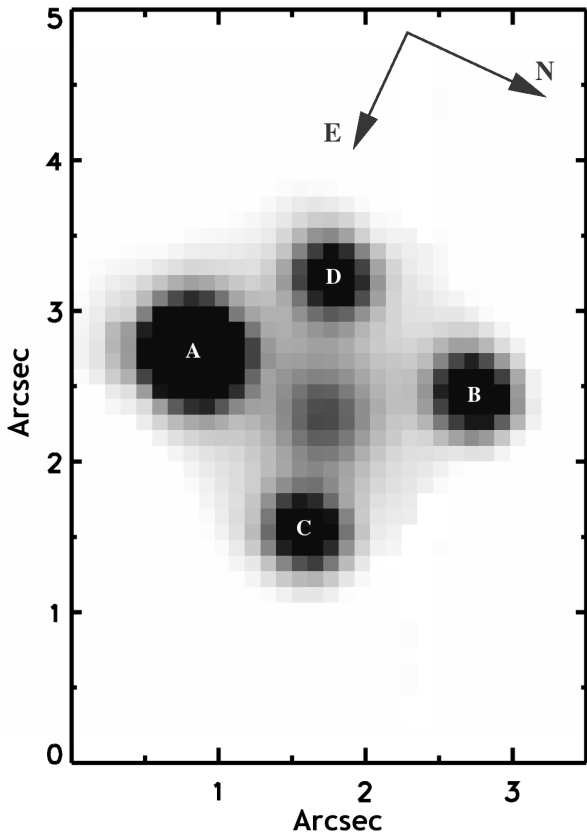


Figure 1. 2-D image created from collapsing ADR-corrected IFU data cube. Letters indicate the standard designation of quasar images in the Einstein Cross.

interpolation between lenslets is required, which makes the determination of brightness ratios significantly more accurate than in the case of non-filled IFUs.

2.1 Data Reduction

The data was reduced using the Gemini IRAF package v1.8, under IRAF v2.12. The standard GMOS IFU reduction recipe was followed for overscan subtraction and trimming, bias subtraction, dark subtraction, flatfielding, arc calibration, spectrum extraction, sky subtraction, and flux calibration. We used calibration files taken as part of the standard Gemini Facility Calibration Unit (GCAL) suite.

Cosmic ray removal was performed separately on the reduced images before spectrum extraction, using CRREJ algorithm via IMCOMBINE. CRREJ performs iterative rejection of unusually high pixels, accounting for the noise properties of the image. In W05 we found that this method provided far superior cosmic ray rejection to that provided by GSCRREJ, and demonstrated the advantage of taking multiple GMOS IFU exposures at the same offset position, as opposed to using an extensive dither pattern. We converted the hexagonal image arrays into rectangular arrays with $0''.1$ square pixels using GFCUBE.

Atmospheric differential refraction (ADR) was found to cause a $0''.8$ shift over the wavelength range. This was corrected by first computing the shifts relative to the

image position at the central wavelength of CIII] using cross-correlation, then fitting a physical model of ADR (Schubert & Walterscheid 2000) to these shifts. The cube was corrected according to the best-fit ADR model.

Figure 1 shows the ADR-corrected data cube collapsed into a 2-D image. The four quasar images and the core of the lensing galaxy are well-resolved.

2.2 PSF Construction and Extraction of Image Spectra

The excellent seeing allows us to extract the spectrum of each quasar image with high precision. Nonetheless, there is some blending between adjacent quasar images and with the core of the lensing galaxy, and so deblending is required.

To deblend, we perform least-squares fitting of the spatial frame at each wavelength element. With positions determined from archival HST imaging, we fit a reconstructed Point Spread Function (PSF; see below) to all quasar images and the galaxy core using χ^2 minimization. For each quasar image, we perform PSF-subtraction of all other quasar images and the galaxy core using the best-fit amplitudes. We then determine the flux for each image, at each wavelength element, within an integration aperture, normalized by the fraction of the model PSF within this aperture. This aperture is a $0''.8$ radius circle centred on the relevant quasar image or galaxy, excluding regions within $0''.8$ of any other quasar image or the galaxy core.

The PSFs used in these fits are determined using an iterative process. As the PSF is wavelength-dependent, we calculate ten different PSFs across the wavelength range, each from a $\sim 100\text{\AA}$ wide stacked frame. The PSF extraction proceeds as follows:

- a.* Take the azimuthal average for each quasar image within $1''.6$ circles, excluding regions within $0''.8$ of any other quasar image or of the galaxy core. This yields four 1-D PSF profiles. We splice these together to construct a single PSF profile and convert this into a azimuthally symmetric 2-D PSF.
- b.* Perform least-squares fitting to obtain a first estimate of quasar image and galaxy core amplitudes.
- c.* Create four frames; in each one, three of the quasar images and the galaxy core are subtracted according to the best-fit normalizations from step *b*, leaving a single quasar image remaining.
- d.* Use these four frames to splice together a 2-D estimate of the PSF using the same regions defined in step *a*.
- e.* Repeat steps *c* through *d* using the 2-D PSF.
- f.* Repeat until the PSF converges, with RMS differences between iterations of $< 0.1\%$.

Using this process, the PSF converged within 5 iterations for all ten 100\AA wavelength bins, and was stable for further iterations.

Figure 2 illustrates the regions used for construction of the PSF and spectral extraction (left), and the residuals after final subtraction for the spectral region of the CIII] line. Figure 3 shows the extracted spectra of the four quasar images.

The use of the PSF to model the core of the lensing galaxy introduces some error. If we assume a de Vaucouleurs' effective radius of $3''.1$ (Schmidt *et al.* 1998), we find that

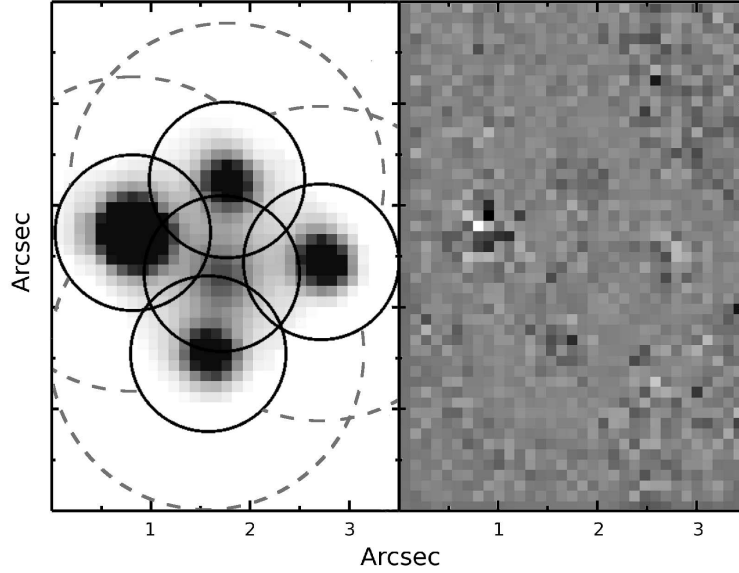


Figure 2. *Left:* Each spectrum is extracted from a $0''.8$ aperture centred on the relevant quasar image or the lensing galaxy core (solid circles), but excluding regions overlapping any other $0''.8$ aperture. The model PSF is constructed with contributions from each quasar image, using $1''.6$ apertures (dashed circles), and again excluding regions within $0''.8$ of other images or the galaxy core (see Sect. 2.2 for details). *Right:* the residual map around the CIII] line after the best-fit subtraction of the constructed PSF from each quasar image and galaxy core. The median of the absolute noise-weighted residuals is $\sim 0.2\sigma$, with a range of $\pm \sim 2\sigma$

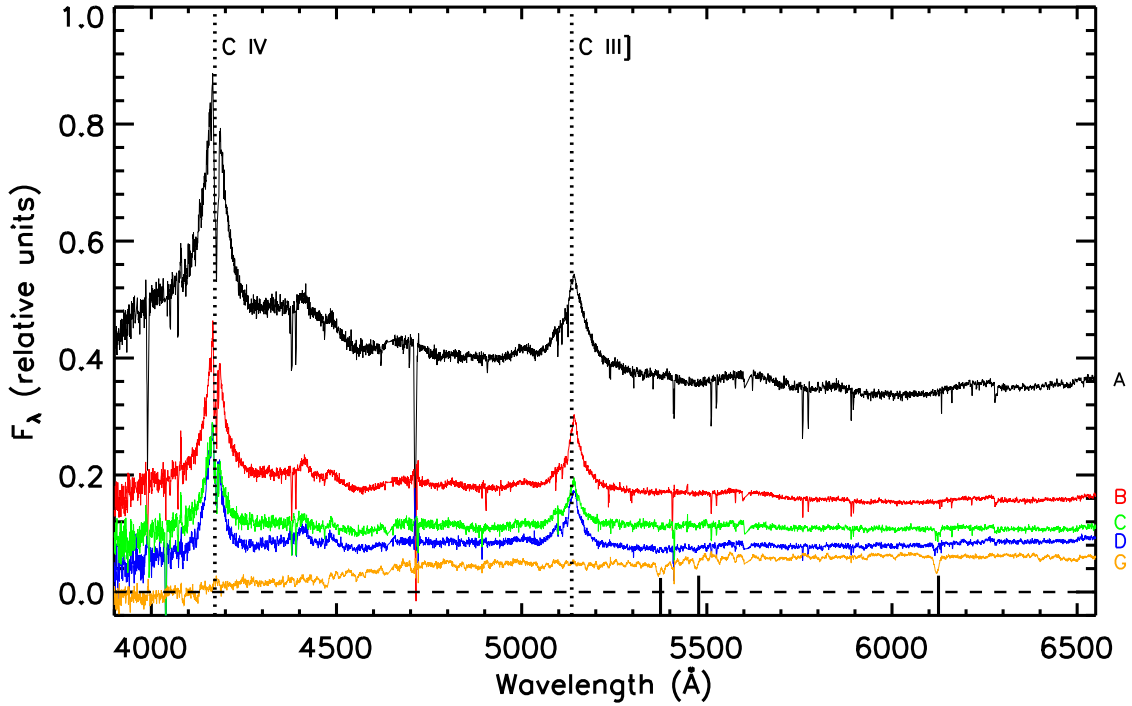


Figure 3. Extracted spectra for the four quasar images and the lensing galaxy in Q2237+0305: black: image A, red: image B, green: image C, blue: image D, orange: lensing galaxy. Dashed lines mark positions of C IV and C III] broad emission lines. Solid vertical lines indicate positions of galaxy absorptions lines, from left to right: Mg b, Fe II, and Na D

the difference in galaxy flux between the de Vaucouleur and PSF models in the integration aperture of images A and B is less than 1% of the quasar image flux in this region. As the galaxy spectrum is reasonably smooth in the region of the CIII] line, any residual galaxy flux is largely removed in the continuum subtraction (see Section 3.3).

3 FLUX AND SPECTRAL RATIOS

In a multiply-imaged quasar, differential microlensing is characterized by a variation in the magnification levels of different spectral components in a single lens image, compared to the “true”, unmagnified quasar spectrum. This effect is most easily observed in the ratio of lens images. In the absence of microlensing, we expect emission line and continuum flux ratios to be equivalent to each other and to agree with the macro-model flux ratios, and we also expect flat, featureless spectral ratios. Gravitational lensing of a point source is achromatic, and so the spectral differences resulting from differential microlensing can be identified independently of the lens model. However it is important to consider the other processes that can also lead to spectral differences between lens images.

3.1 Differential Extinction and Intrinsic Variability

It is possible that extinction properties differ significantly between the lines of sight of each quasar image; both within the lensing galaxy and in intervening absorbing systems. However in this analysis we are concerned with the relative strengths of the continuum and BELR within a small wavelength range (the width of the emission line), and so differential extinction will not be a significant effect. Nonetheless, we correct for extinction using the A_V values of Agol, Jones & Blaes (2000), which uses the average Milky Way extinction curve to obtain A_V for images A of 0.88 ± 0.21 , B of 0.84 ± 0.20 , C of 1.30 ± 0.31 , and D of 1.15 ± 0.27 .

Intrinsic variation within the quasar coupled with time delays between lens images can result in time-varying spectral differences, possibly duplicating the effect of differential microlensing if the continuum undergoes significant variation over a timescale smaller than that of the time delay. In the case of Q2237+0305 the time delay predicted by modeling is less than a day (Kent & Falco 1988), and Chandra observations measure a delay between images A and B of ~ 3 hours (Dai *et al.* 2003). This is sufficiently smaller than the estimated accretion disk light-crossing time of ~ 6 days to eliminate the possibility of significant spectral differences due to intrinsic variation.

3.2 Flux Ratios

Table 1 gives the flux ratios in the CIV and CIII] emission lines and in the continuum. Line ratios use the integrated, continuum-subtracted line fluxes, while continuum ratios use the the continuum level at the central wavelength of each line, determined by a linear interpolation from either side of each line. From these ratios it is apparent that image A is magnified relative to the other images.

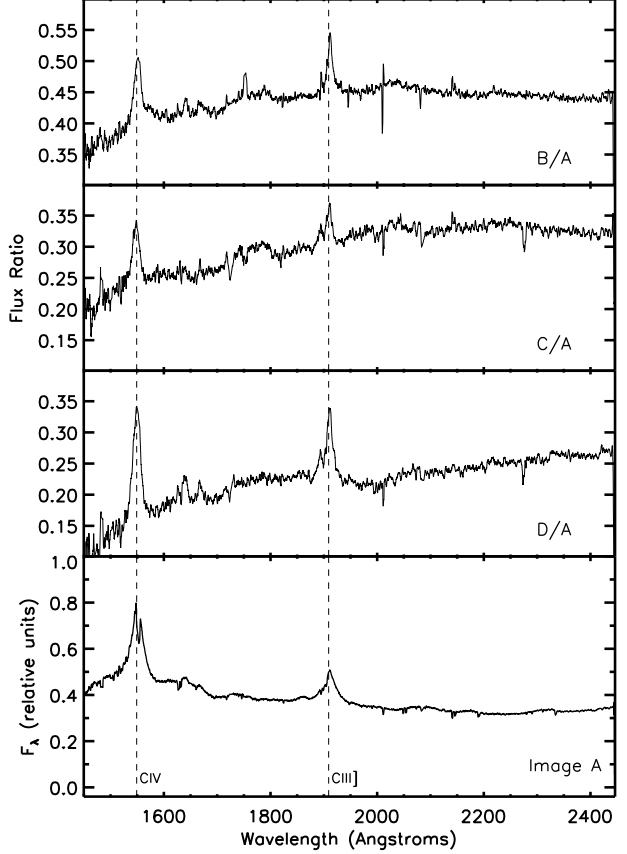


Figure 4. Ratios of spectra for images B, C, and D to image A. Residual features at locations of broad emission lines CIV and CIII] (dashed lines) reveal differential microlensing in which the continuum in image A is magnified relative to the BELR.

Table 1. Flux ratios for CIII] and CIV broad emission lines and for the continuum at the central wavelengths of these lines. Mid IR flux ratios from Agol, Jones & Blaes (2000), radio flux ratios from Falco *et al.* (1996), $H\beta$ from Metcalf *et al.* (2004).

Region	B/A	C/A	D/A
CIII] line	0.569 ± 0.022	0.643 ± 0.025	0.630 ± 0.026
CIII] cont.	0.431 ± 0.026	0.443 ± 0.027	0.281 ± 0.018
CIV line	$0.473 \pm 0.00; 020$	0.454 ± 0.020	0.422 ± 0.021
CIV cont.	0.375 ± 0.034	0.347 ± 0.033	0.203 ± 0.025
Mid IR	1.11 ± 0.11	0.59 ± 0.09	1.00 ± 0.10
8 GHz	1.08 ± 0.27	0.55 ± 0.21	0.77 ± 0.23
$H\beta$ line	0.376 ± 0.007	0.387 ± 0.007	0.461 ± 0.004

We also see differential microlensing between the BELR and the continuum, with the continuum magnified to a greater extent than the BELR. This is expected: given any level of differential microlensing, the smaller emission region should exhibit the most extreme deviation from the macro-model magnification. Using a method similar to that used in W05, we find a size limits for the CIII] BELR of $< 0.066h_{70}^{1/2}$ pc and for the continuum emission region of $< 0.059h_{70}^{1/2}$ pc, both at the 95% confidence level. Note that,

while the limit on the BELR size is similar to that found from our 2002 data, the continuum limit is less tight than the limit of $< 0.02h_{70}^{1/2}$ pc reported in W05. This is because the earlier microlensing event resulted in stronger magnification of the continuum — possible only for smaller accretion disk sizes. Our continuum size limit is also consistent with, but less tight than, the limits found by Pointdexter & Kochanek (2010) and Eigenbrod *et al.* (2008b).

We omit the CIV line from this analysis due to the difficulty in performing an accurate continuum subtraction at the far blue end of the spectrum.

3.3 Spectral Ratios

Figure 4 shows the spectral ratios of each quasar image relative to image A. The presence of features around 1549Å and 1909Å illustrates the differential microlensing between BELR and continuum. The narrowness of these features suggest that there may be differential microlensing across the velocity structure of the line. In the case of a static magnification difference between line and continuum we would expect a broad feature covering the extent of the emission line. We also note that the continuum spectrum of image A is bluer than that of the other images, indicating possible differential microlensing across the accretion disk.

To investigate differential microlensing within the broad line region, we look at the continuum-subtracted emission line ratios. The continuum spectrum at each line is approximated as the linear fit to a 120Å-wide region centered on the line, masked in the central 80Å-wide region. Figure 5 shows the continuum-subtracted CIV and CIII] lines for images A and B (upper plots) and the continuum-subtracted line ratios (lower plots), which are equivalent to emission line magnification ratios.

Errors in the spectral line ratios are derived from uncertainties in the PSF fits (see Sect. 2.2), which take into account errors in subtraction of other images and of the lensing galaxy. We include the error in continuum subtraction, determined conservatively from the error in the linear fit around each line — both from the fit itself and from the variation in the continuum level from fitting to different spectral regions. For the simple analysis to follow, we don't directly calculate the error due to contamination by any iron lines beneath the broad emission lines. Instead we assume that this uncertainty is small compared to the uncertainty in the continuum. We have no direct means to test this assumption.

Both the CIV and the CIII] line ratios reveal a symmetric trend in the magnification ratio about the line centre. This trend is highly significant for the CIII] line. While the trend is apparent for the CIV line, the difficulty in continuum subtraction for this line (see Sect. 3.2) dramatically increases the uncertainty in the spectral line ratios, and so we restrict further analysis of this differential microlensing feature to the CIII] line.

At low velocities near the line centre, the CIII] broad line in image A is magnified compared to the macro-model expectation: $B/A \sim 0.65$ compared to the expected $B/A \sim 1.0$. As line velocity increases this magnification ratio drops further, towards the continuum ratio of $B/A \sim 0.4$. The observed trend suggests that the lower velocity broad line emission samples a region of the caustic structure closer to

the average macro-model magnification level for image A than both the higher velocity gas and the continuum. This in turn suggests that size of the emission region approaches that of the continuum region with increasing gas velocity. Note that this feature cannot be explained by differential microlensing between the narrow line region versus the BLR as the width of the feature exceeds 20Å, or ± 1500 km/s. In the next section we analyse this microlensing signature in the context of simple models of BELR kinematics.

4 MODELS OF THE BELR

We test simple models for two of the physical processes that are considered to be the primary candidates as the dominant drivers of BELR kinematics: an outflow driven by radiation pressure and orbital motion driven by gravity. The aim of these models is to simulate the expected wavelength-dependent surface brightness distributions for these models, and then, by convolving these with simulated magnification maps for Q2237+0305, to determine the expected magnification ratios as a function of wavelength, which we will compare to the observed microlensing signature.

4.1 The Outflow Model

For our simple outflow model we assume a radial wind in twin conical shells. Drawing on the wind model of Elvis (2000), we consider optically thick clouds driven outwards by radiation pressure, with each cloud sufficiently small cross-sectional area to allow us to ignore self-shielding. Under these assumptions we may use the derivation of Capriotti *et al.* (1980), which gives the acceleration of a cloud due to radiation pressure as:

$$a_{rad} = \frac{A_c L}{4\pi c r^2 M_c} \quad (1)$$

where A_c is the cross-sectional area of the cloud, M_c is its mass, L is the total ionising luminosity, and r is the distance from the ionising source. Velocity as a function of radius is therefore:

$$v dv = \frac{A_c L}{4\pi c r^2 M_c} dr \quad (2)$$

So for a starting velocity v_0 at an initial radius r_0 we have:

$$v(r) = \sqrt{\left(\frac{K + r_0 v_0^2}{r_0} - \frac{K}{r}\right)} \quad (3)$$

where $K = A_c L / 2\pi c M_c$. And the terminal velocity, at $r \rightarrow \infty$, is $v_T = \sqrt{(K + r_0 v_0^2)/r_0}$.

At a given projected distance from the centre, x , we know $v_{los} = v \sqrt{1 - \frac{x^2}{r^2}}$. So from equation 3, the radius at which a given v_{los} occurs along a given line of sight satisfies the cubic:

$$f(a) = a^3 - \frac{a^2}{r_0} - \frac{a}{x^2} + \left(\frac{1}{x^2 r_0} - \frac{v_{los}^2}{x^2 K}\right) = 0 \quad (4)$$

where $a = 1/r$. This function yields a single physical solution for the distance from the ionising source of clouds with projected velocity v_{los} at a given projected distance from the centre, x .

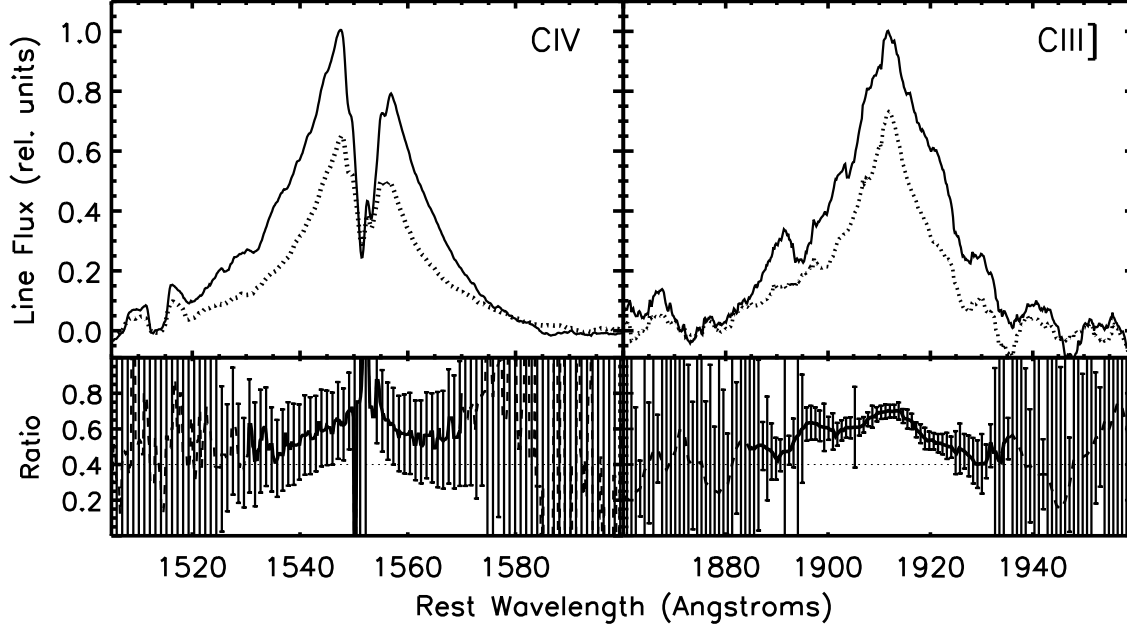


Figure 5. *Upper:* continuum-subtracted CIV and CIII] emission lines for images A (*solid*) and B (*dotted*). *Lower:* B/A ratios using continuum-subtracted emission lines. Solid lines show regions with significant line flux, while dashed lines show regions heavily dominated by noise. Dotted line shows the B/A continuum flux ratio.

We wish to determine the expected surface brightness distribution produced by such a wind as a function of wavelength. If we assume that broad line clouds re-emit a constant fraction of the incident ionising flux in the emission line, then the surface brightness of an emission line at $\Delta\lambda$ from its rest wavelength and at projected distance x from the centre is:

$$\mu_{x,\Delta\lambda} \propto \frac{d\delta x^2\delta z}{r^2} \quad (5)$$

where d is the number density of broad-line clouds at r , δx is the size of the spatial bin, and δz is the distance along the line of sight over which the emission line is shifted into our spectral resolution bin, assumed to be small compared to r . For a spherical outflow, if we assume cloud conservation (i.e. their lifetime is long compared to the flow timescale), then d satisfies: $d \propto 1/(vr^2)$. The size of projected spatial bins, δx , is constant, and so:

$$\mu_{x,\Delta\lambda} \propto \frac{\delta z}{vr^4} \quad (6)$$

So combined with equation 3 we have surface brightness at x and $\Delta\lambda$ as a function of the distance from the source at which that emission is produced. For the purpose of the model it is useful to parameterize K in terms of r_0 , v_0 , and v_T :

$$\mu_{x,\Delta\lambda} \propto \frac{\delta z}{\sqrt{(v_0^2 - v_T^2) \frac{r_0}{r} + v_T^2}} \quad (7)$$

where r and δz are calculated using equation 4.

We include both axial and equatorial obscuration with varying opening angles to simulate constrained winds or obscuration by jet and disk/torus. The final model of a three-dimensional axially symmetric radial wind is parameterized by: launching radius, terminal velocity (which encompasses

cloud properties and continuum luminosity), orientation of the axis to the line of sight, and the opening angle of axial and equatorial black-out regions.

Figure 6 shows an example set of surface brightness distributions for the wind model. As can be seen, significant asymmetries arise for axis orientations not perpendicular to the line of sight. Any obscuring disk or jet quickly blacks out the entire receding wind as velocity increases, and this obscuration increases with smaller orientation angles. Interestingly, the size scale of the surface brightness distribution does not change dramatically with gas velocity, although the red- and blue-shifted high velocity gas is offset in the plane of the sky for low orientation angles. Such offsets are likely to lead to strong differential microlensing, and hence asymmetries between red- and blue-shifted line ratios.

4.2 The Orbital Model

To study the expected microlensing signature of an orbital BELR, we assume a purely Keplerian model consisting of randomly-oriented circular orbits. In this case the analog of equation 4:

$$f(a) = x^2 a^3 - a^2 - \frac{v_{los}^2}{K'} = 0 \quad (8)$$

where $a = \frac{1}{r^2}$, $K' = \frac{GM_{BH}}{2\pi^2}$, and as previously x is the projected distance from the centre and v_{los} is the line-of-sight velocity that we're interested in. The solution to this cubic gives us the radius at which v_{los} occurs for the current x .

We follow the same approach as for the wind model, except that the cloud number density can't be constrained by simple conservation arguments, and so we need to choose a

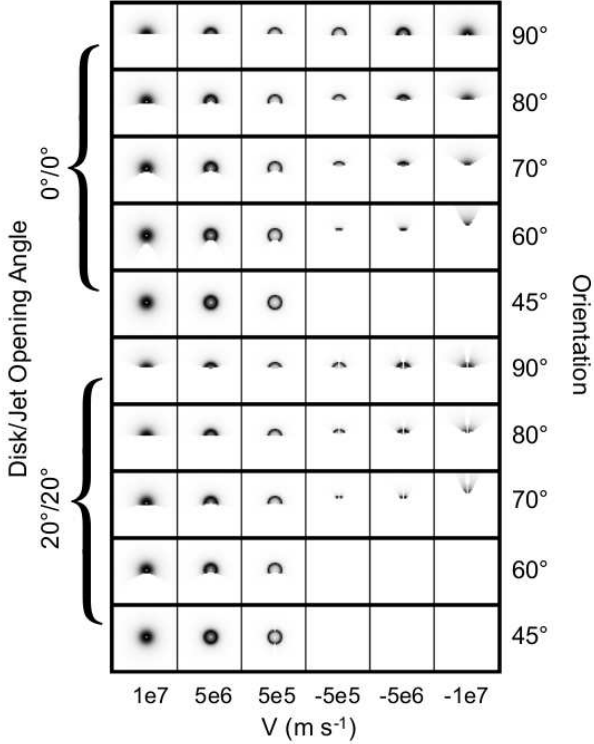


Figure 6. Outflow model surface brightness maps for a selection of the explored parameter space. The depicted models have launching radius $r_0 = 1 \times 10^{16}$ cm and a range of disk/jet opening angles and orientations of the axis to the line of sight. For each parameter set, a small selection of the calculated velocity slices are shown, with negative velocities indicating the receding outflow. The surface brightness peak of the receding outflow is increasingly displaced relative to the approaching outflow as velocity increases. An obscuring disk and jet blacks out a larger fraction of the receding wind as orientation angle decreases and velocity increases, completely blacking out even lower velocity gas at angles below 60° to 70° . Each frame size is 3×10^{17} cm.

density gradient, $d \propto r^\alpha$. We choose a value of $\alpha = -1$, in the mid-range of the mid-range of likely values (e.g. Goad *et al.* 1993).

The surface brightness distribution of a purely Keplerian BELR is then:

$$\mu_{x,\Delta\lambda} \propto K' \delta z r^{\alpha-2} \quad (9)$$

The final model of a spherical BELR comprised of random circular Keplerian orbits is parameterized by: black hole mass, density gradient, orientation of the axis to the line of sight, and the opening angle of axial and equatorial black-out regions.

Figure 7 shows an example set of surface brightness distributions for the orbital model. This model produces symmetric surface brightness distributions for the red- and blue-shifted gas.

4.3 Parameter Range

For both the outflow and the orbital model we include obscuration caused by an equatorial disk and an axial jet. We explore the following disk/jet opening angles for these: $0^\circ/0^\circ$,

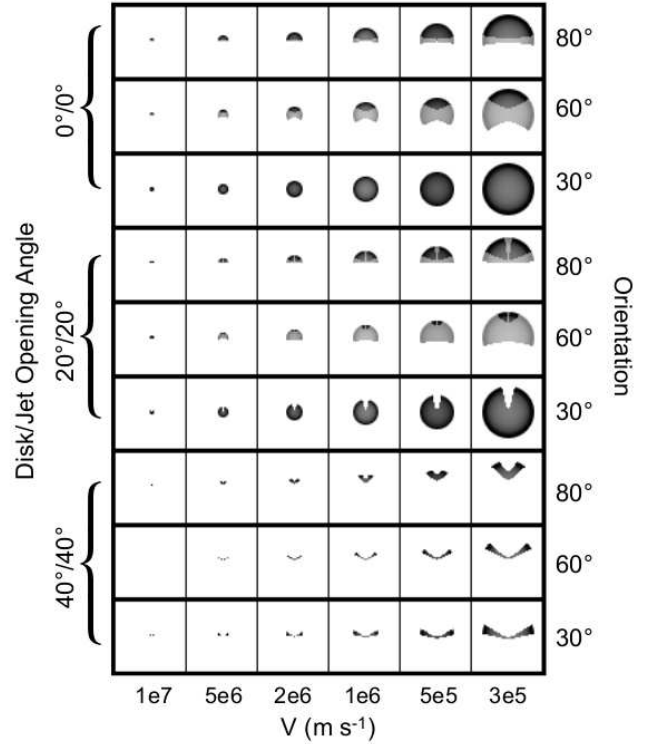


Figure 7. Orbital model surface brightness maps for a selection of the explored parameter space. The depicted models have black hole mass $m_{BH} = 1 \times 10^9 M_\odot$ and a range of disk/jet opening angles and orientations of the axis to the line of sight. For each parameter set, a small selection of the calculated velocity slices are shown. Receding and approaching gas produces symmetrical surface brightness distributions. Each frame size is 3×10^{17} cm.

$0^\circ/10^\circ$, $10^\circ/0^\circ$, $10^\circ/10^\circ$, $40^\circ/40^\circ$, $T/0^\circ$, $T/10^\circ$. “T” indicates a transparent accretion disk; in all other cases the disk is opaque, meaning that only the near side of the BELR is visible.

For both the kinematic models and all opening angle combinations we explore the following orientations: 0° , 15° , 30° , 45° , 60° , 70° , 80° , 90° ;

For the outflow model we simulate wind launching radii r_0 of 1×10^{15} cm, 3×10^{15} cm, 1×10^{16} cm, 3×10^{16} cm, and 6×10^{16} cm. We assume an initial velocity of $v_0 = 0$ and a terminal velocity for the wind of $V_T = 0.1c$

For the orbital model we simulate black hole masses m_{BH} of $1 \times 10^8 M_\odot$, $3 \times 10^8 M_\odot$, $1 \times 10^9 M_\odot$, $1.5 \times 10^9 M_\odot$, $2 \times 10^9 M_\odot$, $3 \times 10^9 M_\odot$, $4 \times 10^9 M_\odot$, and $6 \times 10^9 M_\odot$. We assume a density gradient of $\alpha = -1$.

For each model and parameter combination we calculate surface brightness maps for 5\AA -wide wavelength bins around the CIII] central wavelength between 1809\AA and 2009\AA .

5 MICROLENSING SIMULATIONS

To determine the microlensing signatures predicted by these BELR models, we perform a Monte Carlo simulation in which we convolve the model surface brightness maps with simulated magnification maps to produce a large set of expected line ratio spectra.

The magnification maps are constructed using an inverse ray-shooting technique (e.g. Kayser, Refsdal & Stabell 1986; Wambsganss, Paczyński & Katz 1990a). The key parameters for such simulations are the convergence κ_{tot} and the shear γ of the lens at the image positions. The Q2237+0305 lens model is provided in Table 2 (Trott & Wayth, priv. comm., based on models of Trott *et al.* 2010). We assume a smooth matter component in the lens of 0%, and so the convergence is provided solely by a clumpy stellar component. This is reasonable as the lensed images in Q2237+0305 lie very close to the bulge of the lensing galaxy, where the stellar component is assumed to dominate (Kent & Falco 1988; Schneider *et al.* 1988; Schmidt, Webster & Lewis 1998; Trott *et al.* 2010). A fixed microlens mass of $1M_{\odot}$ was used. The Einstein Radius changes as the square root of this mass, although clustering of caustics is relatively unaffected.

We generated magnification maps for images A and B. These maps have 2048×2048 pixels, with 5 different pixel scales for each. The scale size corresponds to the scale of the BELR model – which increases with r_0 and M_{BH} – and is chosen to allow sufficient independent positions for the Monte Carlo simulation (see below). Table 3 lists the pixel scale used for the different black hole masses and wind launching radii.

For each BELR model parameter set, we generated surface brightness maps for 38 wavelength bins spanning 200\AA centred on the emission line central wavelength. At each iteration of the Monte Carlo simulation we choose two source positions, one on the image A magnification maps and one on the image B magnification maps. We then convolve the BELR surface brightness maps for all 38 wavelength bins with the magnification maps, centred on these two positions. The resulting pair of magnification spectra yields our magnification ratio spectra for the BELR model, which is equivalent to a continuum-subtracted line flux ratio.

The two magnification map positions are constrained by the observed continuum flux ratio. We first randomly select a source position on the B magnification maps. Source positions on the A magnification map are then randomly selected with the constraint that the B/A magnification ratio for a point source be within 10% of the observed continuum flux ratio $B/A = 0.39$.

The above assumes that the dominant continuum emission region is smaller than the spatial resolution element at each pixel scale. For the smallest pixel scales (map sizes $2.4\eta_0$ and $7.2\eta_0$, corresponding to pixel scales of 2.1 – $6.3 \times 10^{14} h_{70}^{-1/2}$ pc), this gives a continuum size smaller than the upper limit found in Section 3.2. However, these sizes are appropriate to the scale of the BELR models considered. They assume the dominant optical continuum emission arises from a region at a factor of ~ 3 or more smaller than the smallest scale of broad-line emission.

We generated 1215 line ratio spectra per wind model, 4860 line ratio spectra for the $M_{BH} = 1.5 \times 10^9 M_{\odot}$, $2 \times 10^9 M_{\odot}$ and $4 \times 10^9 M_{\odot}$ orbital models, and 1215 line ratio spectra for all other orbital models. These line ratio spectra could then be compared directly with the observed B/A line ratio spectrum.

Figures 8 and 9 shows a random selection of simulated magnification ratio spectra for the outflow model and the orbital model respectively, for a single parameter combination.

Table 2. Lensing parameters

Image	κ_{tot}	γ	μ_{tot}
A	0.413	0.382	5.034
B	0.410	0.384	4.984

Lensing parameters for images A and B in Q 2237+0305 (Trott & Wayth, priv. comm., based on models of Trott *et al.* 2010).

Table 3. BELR models and magnification maps

Map size	orbital models (M_{bh} in M_{\odot})	wind models (r_0 in cm)
$2.4\eta_0 \times 2.4\eta_0$	1×10^8	1×10^{15}
$7.2\eta_0 \times 7.2\eta_0$	3×10^8	3×10^{15}
$24\eta_0 \times 24\eta_0$	$1 \times 10^9, 1.5 \times 10^9$	1×10^{16}
$72\eta_0 \times 72\eta_0$	$2 \times 10^9, 3 \times 10^9, 4 \times 10^9$	3×10^{16}
$144\eta_0 \times 144\eta_0$	6×10^9	6×10^{16}

Magnification map size, and the corresponding orbital and wind models. η_0 is the Einstein Radius projected on to the source plane: $1.79 \times 10^{17} h_{70}^{-1/2} (M/M_{\odot})^{1/2}$ cm for Q2237+0305.

For outflow model the parameters are: $r_0 = 1 \times 10^{16}$ cm, orientation 70° , disk/jet opening angle $0^\circ/0^\circ$. For the orbital model the parameters are: $M_{BH} = 3 \times 10^9 M_{\odot}$, orientation 0° , disk/jet opening angle $0^\circ/0^\circ$.

6 MEASUREMENT OF BELR KINEMATICS

As illustrated in Figures 8 and 9, the orbital model tends to reproduce the microlensing signature observed in the data more easily than the wind model. To quantify this comparison, we adopt a simple parameterization for the observed microlensing signature, comparing the amplitude and width of the observed hump. Taking the CIII] continuum-subtracted line ratios between images A and B, we compare the amplitude at the rest wavelength of the emission line (designated L) to an equivalent width analog: the integral across the line’s width minus the continuum ratio, divided by L (designated W). This is illustrated in figure 10. This parameterization is useful because it is sensitive to the central amplitude, the integrated strength, and the symmetry of the feature, which together are effective in identifying shapes similar to the observed microlensing signature.

Figures 11 and 12 show L versus W for a selection of the parameter space explored in the simulations. The error bars show the location of the data in this parameterization and the 2σ uncertainty.

Using this parameterization, we can calculate the p-value for the observed microlensing signature with respect to each model. The probability, P , of each model reproducing the observed microlensing signature within 2σ of L and W is the ratio of the number of simulated points within these error bars to the total number of simulations. The p-value is then the integrated probability distribution below P , which is equal to the number of simulation points with a surrounding point density within a 2σ box equal to or lower than the point density of the observed signature, divided by the total number of simulation points. Given these p-values,

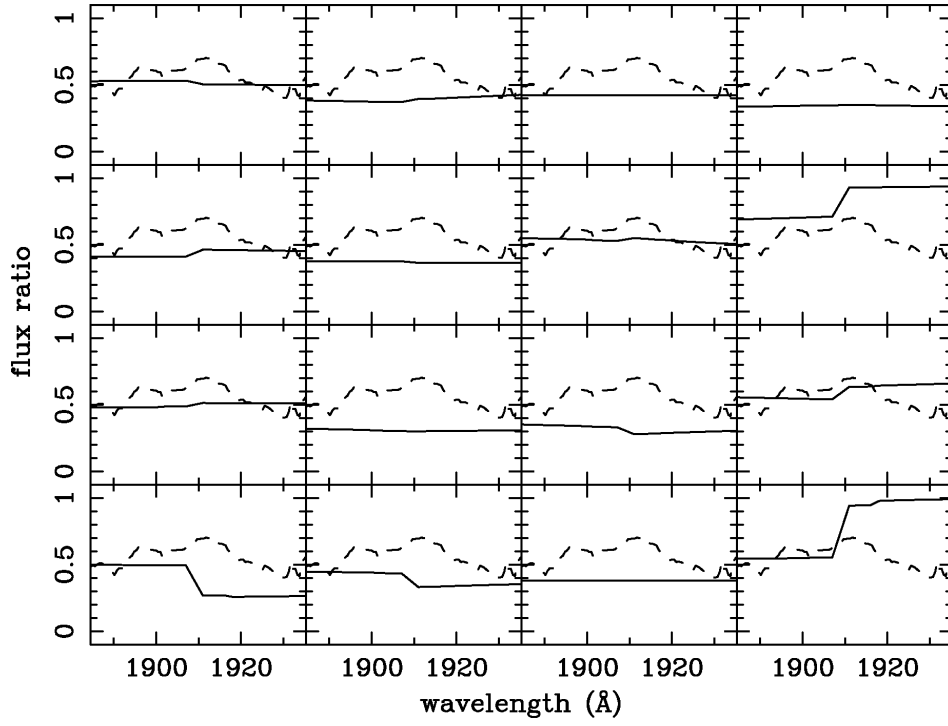


Figure 8. Sample continuum-subtracted line ratios from simulations of outflow model (solid lines), with parameters $r_0 = 1 \times 10^{16}$ cm, orientation 70° , jet/disk opening angle $0^\circ/0^\circ$. Typical microlensing signatures are asymmetric, and the observed hump (dashed lines) is rarely reproduced.

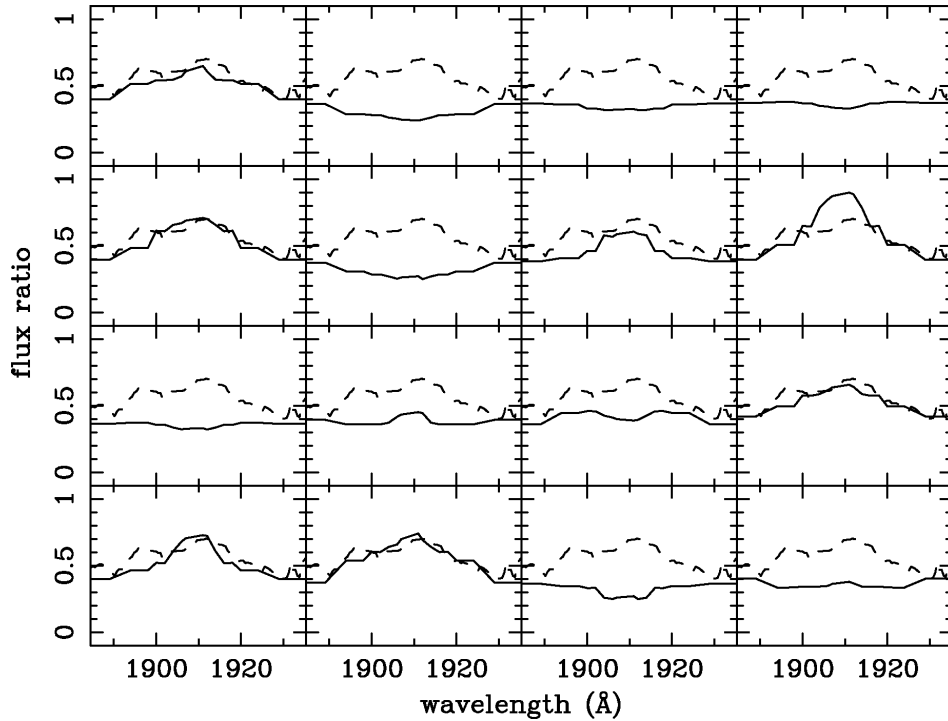


Figure 9. Sample continuum-subtracted line ratios from simulations of orbital model (solid lines), with parameters $r_0 = 3 \times 10^9$ M_\odot , orientation 70° , jet/disk opening angle $0^\circ/0^\circ$. The observed microlensing signature (dashed lines) is similar to the simulations in many cases.

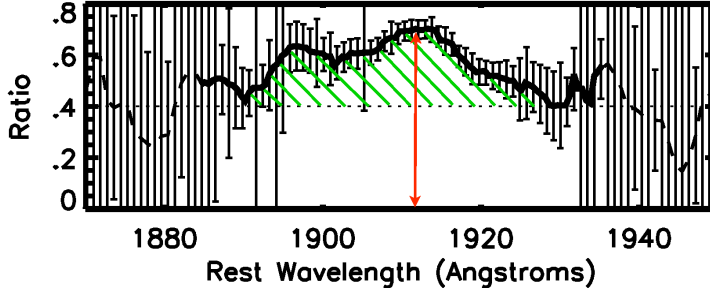


Figure 10. Parameterization of the shape of the observed CIII] microlensing signature: we define W , an equivalent width analog for the ratio of continuum-subtracted line ratio for images B/A: the integrated ratio minus the continuum ratio (green area) divided by L , the central-wavelength amplitude of the ratio (red arrow).

we can reject models and parameter combinations with a quantifiable significance level.

Figure 13 shows the p-values for the orbital model as a function of orientation, for a range of disk and jet opening angles and black hole masses/launching radii. Fig. 13 (right) shows the average probabilities over all orientations as a function of black hole mass/launching radius.

Figure 14 shows the orientation-averaged p-values for both the orbital and the wind models, for all disk and jet opening angles and a selection of black hole masses and wind launching radii.

Assuming the orbital model, the p-value for the observed microlensing signature is inversely proportional to black hole mass. We can place a firm upper limit on black hole mass, assuming this orbital model. Models with $M_{BH} \geq 1.5 \times 10^9 M_{\odot}$ are rejected with $>99\%$ confidence. Larger black hole masses are ruled out for all orientations and disk/jet opening angles.

The most probable disk/jet configuration for all orientations and black hole masses is one with a large opening angle for both disk and jet of 40° . Interestingly, cases where only one of the disk or the jet have a large opening angle are ruled out with $>99\%$ probability.

For the pure outflow model, very few parameter sets are capable of reproducing the observed microlensing signature. All are ruled out with high ($>99\%$) confidence with the exception of models with very small starting radii for the wind (10^{15} cm; probably unphysical as it is smaller than the lower estimates of the accretion disk size, e.g. Eigenbrod *et al.* 2008b) and a tightly constrained orientation range ($\sim 70^\circ$), which are excluded at only the 90% level. This tells us that it is unlikely that a pure accelerating outflow produced the observed microlensing signature.

Changing the mean microlensing mass marginally affects the p-values, but the general results are the same. If mean masses are smaller, differential microlensing becomes less likely but increases in strength, and vice versa for larger mean masses. It becomes no easier to produce the observed microlensing signature with a pure outflow model.

7 DISCUSSION

Reverberation mapping studies have now provided evidence for inflowing, outflowing, Keplerian and virialised motions in

quasar BELRs (Denney *et al.* 2009; Bentz *et al.* 2009). Using a wide range of observational evidence, Gaskell (2009) has argued in favour of infall velocities which are smaller than the Keplerian velocities. Flow-dominated BELR models, for example those outlined by Blandford & Rees (1991) and Elvis (2000) are especially attractive because it is known that high velocity nuclear flows are very common, if not ubiquitous, in quasars. Indeed, the fraction of quasars in SDSS showing some CIV broad absorption is 25% (Trump *et al.* 2006). The line-driven photoionised wind modelled by Murray *et al.* (1995) produced line profiles in good agreement with observation. In addition, there are now strong physical arguments for circular motions (gravity), and also the first observational evidence from polarisation of the H β line (Young *et al.* 2007). Thus there is still no consensus on even the simple question of the direction of the gas flow in the broad line region.

Our analysis shows that a pure Keplerian model for the BELR is able to reproduce the observed microlensing signature. In contrast, our pure accelerating outflow model cannot reproduce this signature for any physical launching radius. This is expected considering the qualitative nature of this signature. The low velocity gas exhibits the strongest differential microlensing relative to the continuum (which is expected to arise from the smallest size scale), while the high velocity gas exhibits flux ratios closer to that of the continuum. This distribution of velocities is consistent with a Keplerian field in which the highest velocities are expected closest to the central gravitating body, but inconsistent with a purely accelerating outflow in which velocity increases with distance.

The observed differential microlensing signature for the BELR is also consistent with that observed blueness of the continuum for image A: if smaller size scales are preferentially magnified, then we expect the continuum to appear more blue, assuming that this magnification gradient extends to scales smaller the outer regions of the accretion disk.

7.1 Implications for Outflow Models

The observed differential microlensing signature rules out BELR models in which the gas dynamics at all radii are dominated by an accelerating outflow. This includes winds that are exclusively driven by line pressure. Other drivers, such as ther-

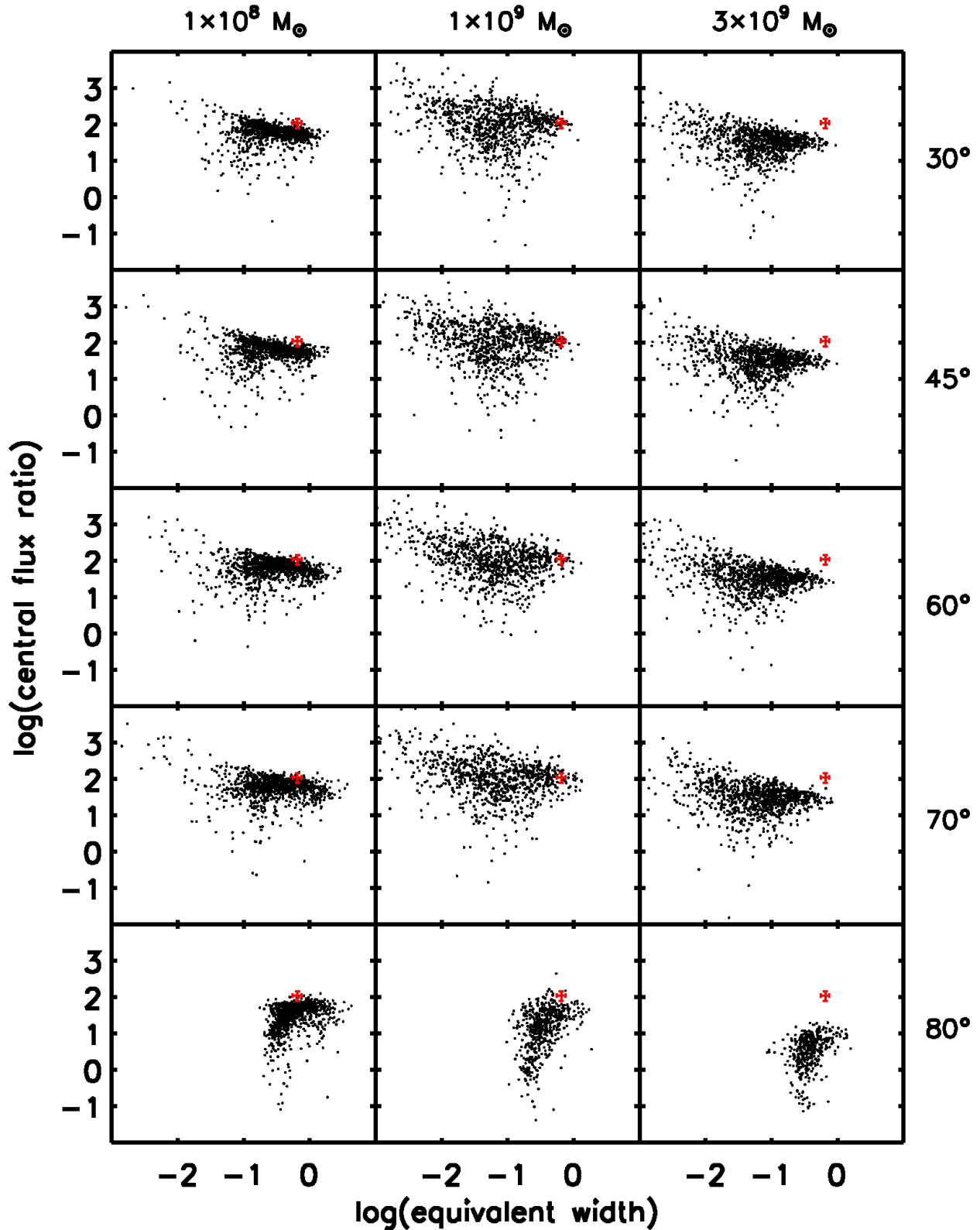


Figure 11. “Equivalent width” of the continuum-subtracted line ratio versus the central flux ratio for simulations (*black points*) and data (*red error bars*). A selection of the explored parameter space is shown: M_{BH} of $1 \times 10^8 M_\odot$ to $3 \times 10^9 M_\odot$, orientations of 30° to 80° , and jet/disk opening angle of $20^\circ/20^\circ$. A black hole mass of $1 \times 10^9 M_\odot$ is favoured, while a black hole mass of $3 \times 10^9 M_\odot$ appears unlikely.

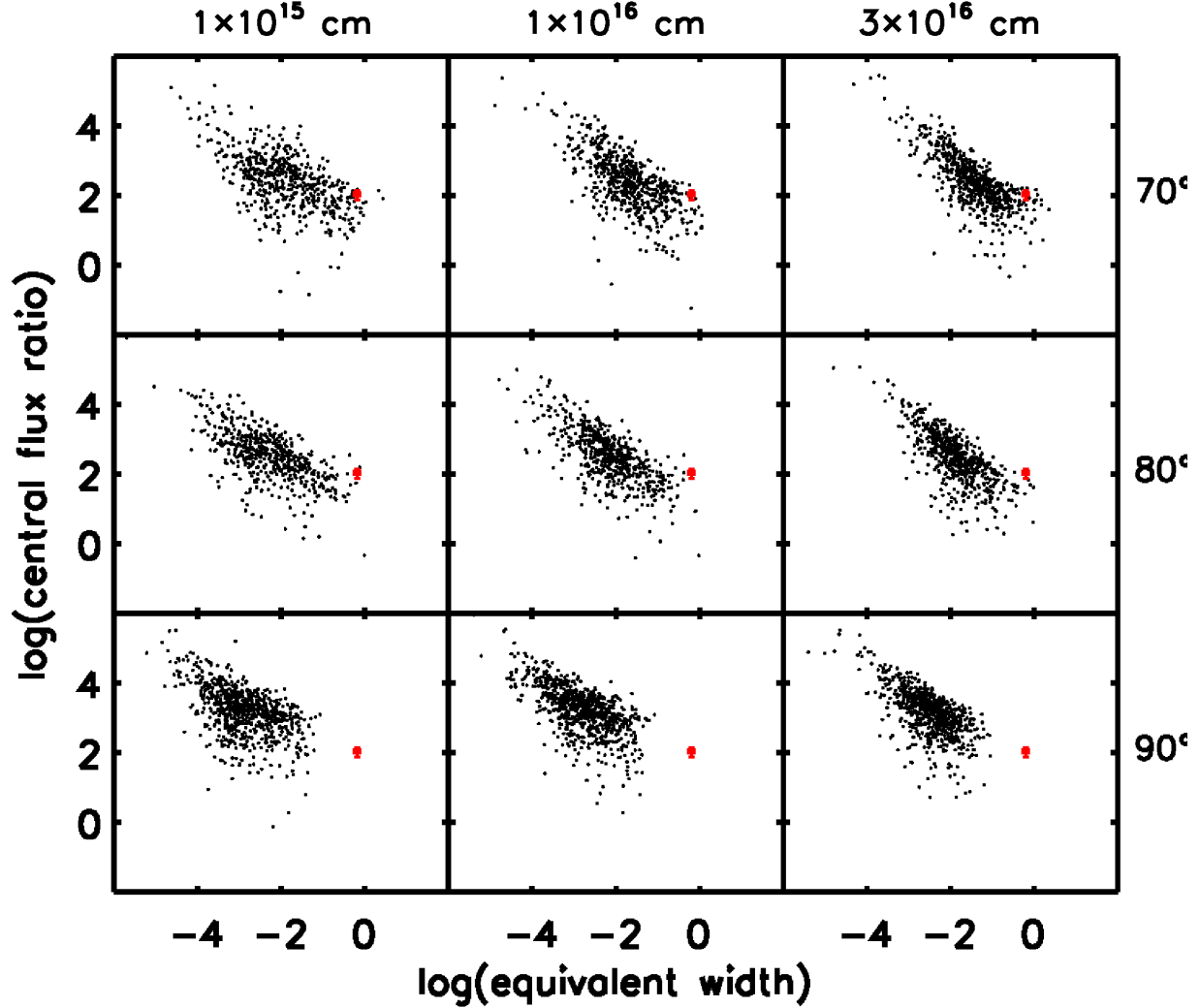


Figure 12. “Equivalent width” of the continuum-subtracted line ratio versus the central flux ratio for simulations (*black points*) and data (*red error bars*). A selection of the explored parameter space is shown: r_0 of 1×10^{15} cm, 1×10^{16} cm, and 3×10^{16} cm, orientations of 70° , 80° , and 90° , and jet/disk opening angle of $20^\circ/20^\circ$. For smaller orientations the data point falls much further from the simulations.

mal expansion of the confining gas (Weymann *et al.* 1982), centrifugal force (Blandford & Payne 1982; Emmering, Blandford & Shlosman 1992) or radiation pressure via dust (Voit *et al.* 1993) may produce outflows in which high velocity gas dominates at smaller radii.

Even if the driving force behind the outflow only allows for an accelerating wind, such models are still viable so long as the gas remains within the gravitationally dominated region for a period comparable to or greater than its orbital period.

7.2 A Pure Keplerian Field?

Until recently, reverberation mapping studies have found that BELR velocity distributions are consistent with Keplerian motion (Peterson & Wandel 2000). Our results are consistent with this, and extend the finding of reverberation mapping—itsself applicable to low-luminosity AGN—

into the high-luminosity regime. Gravitationally-dominated kinematics are also supported by the fact that the AGN black hole masses calculated based on the assumption of a virial BELR follow the $M_{BH}-\sigma_*$ relation of normal elliptical galaxies (Ferrarese *et al.* 2001).

Recent reverberation mapping results with greatly improved velocity resolution have now found evidence for both infall- and outflow-dominated BELR kinematics (Denney *et al.* 2009; Bentz *et al.* 2009), indicating that a variety of dynamical processes are important. Simple randomly oriented orbits are unlikely. It is known that the inner region of quasar BELRs can be as small as 10^{16} cm (Kaspi *et al.* 2000), which overlaps the outer regions of accretion disk. This greatly restricts the possible orbits in the innermost regions of the BELR.

Given the likely presence of multiple kinematic regimes within the BELR, we interpret our results cautiously. Rather than implying a spherical Keplerian field, we instead take

these results to indicate that the inner regions of the BELR are strongly gravitationally dominated, which may include orbital motion and/or infall.

7.3 A Constrained Vortex?

In our simple models, the configuration that most easily reproduces the observed microlensing signature is one in which both accretion disk and jet have large (40°) opening angles; configurations in which only the disk *or* jet have a large opening angle are ruled out with high confidence. Interestingly, this configuration of large opening angles is similar to the hollowed-cone geometry of many wind models. Thus, our modeling suggests that such a geometry is viable, but *only* if the gas motion within this outflow cone is gravitationally dominated at small radii. This is consistent with the vortex model of Elvis (2000), in which line-driven gas outflowing in a hollowed cone initially orbits at accretion disk velocities, or with the magnetically-constrained outflow similar to that proposed by Emmering, Blandford & Shlosman (1992).

This interpretation is also consistent with the biconical model proposed by Abajas *et al.* (2007) to explain the recurrent microlensing enhancement of the broad line blue wings in SDSS J1004+4112.

7.4 Black Hole Mass Limit

Our black hole mass limit of $M_{BH} < 1.5 \times 10^9 M_\odot$ is of similar order to the virial estimate based on the width of the CIV line ($0.9 \times 10^9 M_\odot$; Morgan *et al.* 2010). If we calculate a virial black hole mass from the upper limit on the CIII] BELR from Section 3.2 and the line's velocity FWHM, we instead obtain $M_{BH} < 2 \times 10^8 M_\odot$.

Modeling the differential microlensing signature with a BELR comprised of a simple Keplerian field seems to be as useful for obtaining black hole mass limits based on the virial assumption as the standard method. It has the added advantage of including both BELR velocity and size in the model, instead of using quasar luminosity as a proxy for BELR size (calibrated using low-luminosity quasars). However stronger limits are obtainable by placing a more direct limit on BELR size from microlensing of this region.

7.5 Comparison to Other Works

Eigenbrod *et al.* (2008) also detect differential microlensing within the velocity structure of the BELR in their long-running VLT monitoring campaign. The nature of the signatures are broadly consistent with those we observe; in high-magnification phases, the wings of the CIII] line were more strongly amplified than the core.

Pointdexter & Kochanek (2010) are able to constrain the orientation of the accretion disk of Q2237+0305 by comparing the expected light curve produced by a model accretion disk with the continuum light curve observed over 11 years of OGLE monitoring. Their finding of $\cos i > 0.66$, which is to say a face-on accretion disk within $\sim 50^\circ$ of the line of sight, is consistent with our results, which don't strongly constrain orientation except for a few specific parameter combinations; in particular, Keplerian models with the largest black hole masses (see Fig. 13).

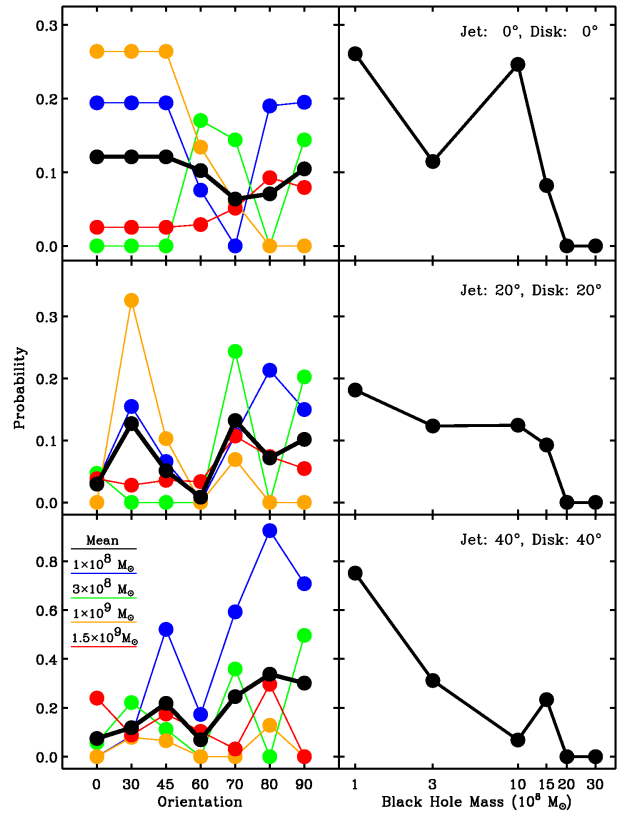


Figure 13. *Left:* p-value as a function of orientation for a range of black hole masses (blue: $10^8 M_\odot$, green: $3 \times 10^8 M_\odot$, yellow: $10^9 M_\odot$, red: $1.5 \times 10^9 M_\odot$), and the average p-value over black hole masses (black lines). *Right:* average p-value over all orientations as a function of black hole mass. Vertical panels show results for different jet/disk opening angles (upper: $0^\circ/0^\circ$, middle: $20^\circ/20^\circ$, lower: $40^\circ/40^\circ$).

8 CONCLUSION

We have presented observations of the gravitationally lensed quasar Q2237+0305 taken with the Gemini North GMOS IFU. Ratios between continuum subtracted image B and image A spectra reveal differential microlensing across the velocity structure of the CIII] broad emission line. The high velocity wings of this line tend towards the flux ratio of the continuum, and the lower velocity core, while still microlensed, is closer to the expected flux ratio in the absence of microlensing. This implies that the high velocity component is emitted from a region with a size comparable to that of the continuum emission region, whereas the low velocity component is emitted from a larger region.

We conducted microlensing simulations using two simple models of the broad emission line region: an outflow model and an orbital model. The outflow model assumes a clumpy wind accelerated by radiation pressure. The orbital model assumes circular Keplerian orbits with random orientations. For both models we tested a wide range of parameters. These models were used to construct an ensemble of simulated B/A flux ratios as a function of velocity, for comparison with the observed flux ratio spectrum.

A purely radial outflow was unable to reproduce the observed differential microlensing signature for any plausible

jet opening angle					disk opening angle	jet opening angle				
Tr	0°	20°	40°			Tr	0°	20°	40°	
black hole mass $10^8 M_\odot$	0.15	0.15	0.16	0.00	0°	0.00	0.00	0.10	0.00	launching radius 10^{16} cm
	0.09	0.09	0.11	0.00	20°	0.00	0.00	0.10	0.00	
	0.00	0.00	0.00	0.43	40°	0.00	0.00	0.00	0.00	
$10^9 M_\odot$	0.05	0.05	0.06	0.00	0°	0.00	0.00	0.10	0.00	3×10^{16} cm
	0.04	0.04	0.05	0.00	20°	0.00	0.00	0.20	0.00	
	0.00	0.00	0.00	0.13	40°	0.00	0.00	0.00	0.00	
random Keplerian orbits						radiation-driven outflow				

Figure 14. Probability of the observed microlensing signature as a function of model parameters. These values are derived by integrating the density functions of the simulated central ratio vs. equivalent width distributions (Figs. 12 and 11) up to the density found at the location of the observed signature. *Left:* orbital model, with probabilities averaged over all orientations. *Right:* outflow model, with probabilities averaged over 70° and 80° orientations only. For all other orientations the outflow model produced no results close to the observed signature for any launching radius.

launching radius of the wind. Conversely, the orbital model was able to reproduce the observed signature for all simulated black hole masses $M_{bh} < 2 \times 10^9 M_\odot$. Though our orbital model is simplistic, we interpret this result as further evidence that the inner regions of the BELR are gravitationally dominated. This is consistent with an outflow model where the BELR gas is lifted off the quasar accretion disk, and thus retains a high Keplerian velocity.

The BELR models presented here are not intended to accurately describe the physical situation in the quasar. They describe only the generic behaviour of a radially outflowing wind, or a collection of orbiting clouds. More sophisticated models, perhaps making use of radiative transfer codes such as CLOUDY, may provide additional constraints on the quasar central engine.

We have obtained Gemini IFU observations of nine other gravitationally lensed quasars, both double and quadruply imaged. These data will allow us to probe a range of quasar orientations, emission lines, black hole masses, and therefore BELR emission region scales. The analyses of these data are forthcoming.

9 ACKNOWLEDGEMENTS

NFB acknowledges the support of an Australian Postgraduate Award.

This paper has been typeset from a \LaTeX file prepared by the author.

REFERENCES

- Abajas, C., Mediavilla, E., Munoz, J. A., Gomez-Alvarez, P., Gil-Merino, R., 2007, *ApJ*, 658, 748
- Agol, E., Jones, B., Blaes, O., 2000, *ApJ*, 545, 657
- Allington-Smith, J., Graham, M., Content, R., Dodsworth, G., Davies, R., Miller, B. W., Jorgensen, I., Hook, I., Crampton, D., Murowinski, R., 2002, *PASP*, 114, 892
- Bate, N. F., Webster, R. L., Wyithe, J. S. B., 2007, *MNRAS*, 381, 1591
- Bentz, M. C., Walsh, J. L., Barth, A. J., *et al.*, 2009, *ApJ*, 705, 199
- Blandford, R. D., Payne, D. G., 1982, *MNRAS*, 199, 883
- Blandford, R. D., Rees, M. J., 1991, in Holt, S. S., Neff, S. G., Urry, C. M., (eds), *Testing the AGN Paradigm*, AIP Conf. Proc. 254, p3
- Capriotti, E., Foltz, C., Byard, P. 1980, *ApJ*, 241, 903
- Congdon, A. B., Keeton, C. R., Osmer, S. J., 2007, *MNRAS*, 376, 263
- Dai, X., Chartas, G., Agol, E., Bautz, M. W., Garmire, G. P., 2003, *ApJ*, 589, 100
- Denney, K. D., Peterson, B. M., Pogge, R. W., *et al.*, 2009, *ApJ*, 704, L80
- Eigenbrod, A., Courbin, F., Sluse, D., Meylan, G., Agol, E., 2008 *A&A*, 480, 647
- Eigenbrod, A., Courbin, F., Meylan, G., Agol, E., Anguita, T., Schmidt, R. W., Wambsganss, J., 2008 *A&A*, 490, 933
- Elvis, M. 2000, *ApJ*, 545, 63
- Emmering, R. T., Blandford, R. D., Shlosman, I., 1992, *ApJ*, 385, 460
- Everett, J. E, 2007, *Astrophys. Space Sci.* 311, 269
- Falco E. E., Lehar J., Perley R. A., Wambsganss J., Gorenstein M. V., 1996, *AJ*, 112, 897
- Ferrarese, L., Pogge, R. W., Peterson, B. M., Merritt, D., Wandel, A., Joseph, C., 2001, *ApJ*, 555, L79
- Gaskell, C. M 2009 *NewAR*, 53, 140
- Goad, M. R., O'Brien, P. T., Gondhalekar, P. M., *MNRAS*, 263, 149
- Hook, I., Jorgensen, I., Allington-Smith, J. R., Davies, R. L., Metcalfe, N., Murowinski, R. G., Crampton, D., 2004, *PASP*, 116, 425
- Huchra J., Gorenstein M., Kent S., Shapiro I., Smith G., Horne E., Perley R., 1985, *AJ*, 90, 691
- Hutsemekers, D., Borguet, B., Sluse, D., Riaud, P., Anguita, T., 2010, *A&A*, 519, 103
- Kaspi, S., Smith, P. S., Netzer, H., Maoz, D., Jannuzi, B. T., Givon, U., 2000, *ApJ*, 533, 631
- Kayser R., Refsdal S., Stabell R., 1986, *A&A*, 166, 36
- Keeton, C. R., Burles, S., Schechter, P. L., Wambsganss, J., 2006, *ApJ*, 639, 1
- Kent, S. M., Falco, E. E., 1988, *AJ*, 96, 1570
- Kochanek, C. S., 2004, *ApJ*, 605, 58
- Lewis, G. F., Ibata, R. A., 2004, *MNRAS*, 348, 24
- Metcalfe, R. B., Moustakas, L. A., Bunker, A. J., Parry, I. R., 2004, *ApJ*, 607, 43
- Morgan, C. W., Kochanek, C. S., Morgan, N. D., Falco, E. E., 2010, *ApJ*, 712, 1129
- Murray, N., Chiang, J., Grossman, S. A., Voit, G. M., 1995, *ApJ*, 451, 498
- Murray, N., Chiang, J., *ApJ*, 474, 91
- Nemiroff, R. J., 1988, *ApJ*, 335, 593
- Peterson, B. M., Wandel, A., 2000, *ApJ*, 540, L13

- Pointdexter, S., Kochanek, C., 2010, *ApJ*, 712, 668
- Proga, D., 2007, in Ho, L. C., Wang, J.-C., (eds), *The Central Engine of Active galactic Nuclei*, ASP Conf. Ser., vol 373, p267.
- Racine R., 1992, *ApJ*, 395, L65
- Schmidt R., Webster R. L., Lewis G. F., 1998, *MNRAS*, 295, 488
- Schneider D. P., Turner E. L., Gunn J. E., Hewitt J. N., Schmidt M., Lawrence C. R., 1988, *AJ*, 95, 161
- Schneider, P., Wambsganss, J., 1990, *A&A*, 237, 42
- Schubert, G., Walterscheid, R. L. 2000, in *Allen's astrophysical quantities*, 4th edition, ed. Arthur N. Cox. (New York: AIP Press), 239
- Sluse, D., Claeskens, J.-F., Hutsemekers, D., Surdej, J., 2008, *RMxAC*, 32, 83
- Trott C. M., Treu T., Koopmans L. V. E., Webster R. L., 2010, *MNRAS*, 401, 1540T
- Trump, J. R., Hall, P. B., Reichard, T. A., Richards, G. T., Schneider, D. P., Vanden Berk, D. E., Knapp, G. R., Anderson, S. F., Fan, X., Brinkman, J., Kleinman, S. J., Nitta, A. 2006, *ApJS*, 165, 1
- Voit, G. M., Weymann, R. J., Korista, K. T., 1993, *ApJ*, 413, 95
- Wambsganss J., Paczyński B., Katz N., 1990, *ApJ*, 352, 407
- Wambsganss, J., Paczyński, B., Schneider, P., 1990, *ApJ*, 358, L33
- Wayth, R. B., O'Dowd, M. J., Webster, R. L., *MNRAS*, 359, 561
- Weymann, R. J., Scott, J. S., Schiano, A. V. R., Christiansen, W. A., 1982, *ApJ*, 262, 497
- Witt, H. K., Mao, S., Schechter, P. L., 1995, *ApJ*, 443, 18
- Wyithe, J. S. B., Webster, R. L., Turner, E. L., Mortlock, D. J., 2000, *MNRAS*, 315, 62
- Wyithe, J. S. B., Loeb, A., 2002, *ApJ*, 577, 615
- Young, S., Axon, D. J., Robinson, A., Hough, J. H., Smith, J. E., 2007, *Nature*, 450, 74